Aqueous Zn Batteries Hot Paper

How to cite: *Angew. Chem. Int. Ed.* **2023,** *62,* e202300823
International Edition: doi.org/10.1002/anie.202300823
German Edition: doi.org/10.1002/ange.202300823

Solid-Adsorbed Polymer-Electrolyte Interphases for Stabilizing Metal Anodes in Aqueous Zn and Non-Aqueous Li Batteries

*Shuo Jin, Yue Deng, Pengyu Chen, Shifeng Hong, Regina Garcia-Mendez, Arpita Sharma, Nyalaliska W. Utomo, Yiqi Shao, Rong Yang, and Lynden A. Archer**

Abstract: Polymers are known to adsorb spontaneously from liquid solutions in contact with high-energy substrates to form configurationally complex, but robust phases that often exhibit higher durability than might be expected from the individual physical bonds formed with the substrate. Rational control of the physical, chemical, and transport properties of such interphases has emerged as a fundamental opportunity for scientific and technological advances in energy storage technology but requires in-depth understanding of the conformation states and electrochemical effect of the adsorbed polymers. Here, we analyze the interfacial adsorption of oligomeric polyethylene glycol (PEG) chains of moderate sizes dissolved in protic and aprotic liquid electrolytes and find that there is an optimum polymer molecular weight of approximately 400 Da at which the highest columbic efficiency is achieved for both Zn and Li deposition. These findings point to a simple, versatile approach for extending the lifetime of batteries.

Introduction

The solid-electrolyte interphase (SEI) is known to play a decisive role in the performance of electrochemical cells operated at voltages outside the reduction limits of electrolyte components.[1] An unstable SEI leads to a variety of well-studied problems that all impact the long-term operation of batteries that use metals as anode. These problems range from mossy/dendritic deposition, poor reversibility, and by-product accumulation.[2] Artificial SEI (ASEI), such as Langmuir–Blodgett graphene layers,[3] MoS_2 layers,[4] and various preformed polymer coatings[5] have been proposed and in some cases demonstrated to be highly effective in stabilizing the interfacial properties and improving long-term cycling performance of metal anodes. Among these approaches, ASEI formed by adsorption of polymer additives at a high-energy electrode surface stands out as a good and desirable tool to regulate the interfacial properties of metal electrodes in terms of ease of application and scale-up.[6] Polymer additives that do not appreciably alter the ionic conductivity of the electrolyte may also be added in excess to spontaneously form interphases at a metal electrode with desirable, self-repair/healing features that might enhance long-term stability of essential electrolyte components in the reducing environment at a metal anode. This feature is also important because it provides a hypothetical mechanism for creating interphases that are chemically and mechanically stable enough to accommodate the cyclic changes in volume inherent to most rechargeable batteries that utilize metals as anodes.[5a,7]

To explore the relationship between spontaneous polymer adsorption from liquid electrolytes on the reversibility of metal electrodes, we investigated physical and electrochemical properties of electrolytes containing polymers with varying molecular weights, M_w. Figure 1a illustrates the adsorption/desorption process for a single polymer chain at a weakly adsorbing planar substrate. The process is thought to occur in two steps: Step 1, a molecular-weight dependent entropic force draws polymer chains in solution end-first, towards the substrate.[8] Step 2, the remaining segments of the polymer chains are able to overcome the free-energy barrier of adsorption (ΔG), enabling the whole polymer chain to adsorb.[18] We note that ΔG is a combination of a configurational entropy (ΔS) and distance-dependent enthalpy (ΔH) term,[9] which is itself a balance between the strength with which chain segments are attracted to the solid electrode substrate and to the liquid electrolyte solvent. For polymers dissolved in good solvents, desorption is competitive with adsorption, and the interphases formed by polymer adsorption are expected to be thin, molecular-weight dependent, and dynamic.[8a,b,10]

For low M_w polymers, end-groups dominate and ΔG is primarily determined by the enthalpic effects. At a high-energy substrate, polymer adsorption from a good solvent is weak and therefore the dynamics are set by the chain-end mobility. This means that the adsorbed layer may be thought of as fluid-like on most timescales, with polymer chains shuttling between adsorbed, solid-like, and liquid-like solution states, on timescales similar to those of isolated chains in solution. For high M_w polymers, the end-effect is less important and entropic forces drive adsorption in a classic loop-train-tail configuration in which the train segments adsorb to multiple sites on the substrate, dramatically

[*] S. Jin, P. Chen, R. Garcia-Mendez, A. Sharma, N. W. Utomo, Y. Shao, R. Yang, L. A. Archer
Robert Frederick Smith School of Chemical and Biomolecular Engineering, Cornell University
Ithaca, NY 14853 (USA)
E-mail: laa25@cornell.edu

Y. Deng, S. Hong
Department of Materials Science and Engineering, Cornell University
Ithaca, NY 14853 (USA) 44434

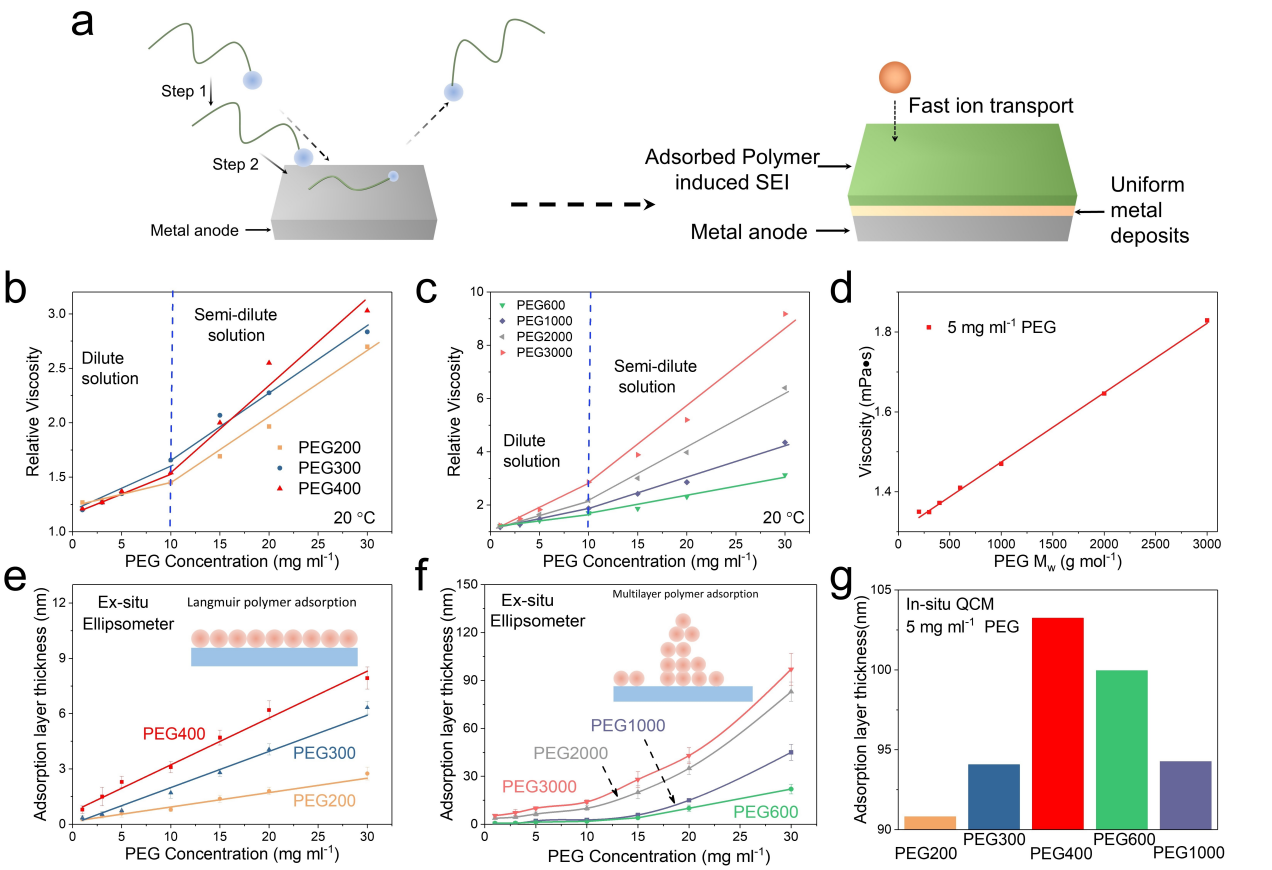

Figure 1. a) Schematic illustrating the single-polymer chain adsorption/desorption process and the corresponding SPEI formed at a metal anode. The gray flat plate represents the metal anode. Green linear chains represent the backbone of the adsorbed polymer and blue balls represent the end-group of the polymer. Step 1: end-group contacts with the high-energy metal surface; step 2: the whole polymer conforms at the metal surface. The green layer represents the SPEI layer, in which *h* represents the average adsorption thickness. The yellow layer represents the metal electrodeposits. b) PEG concentration versus Viscosity curve in PEG200, PEG300 and PEG400 solutions. The two linear lines indicate the dilute and semi-dilute regions of polymer electrolytes. c) Concentration versus Viscosity curve in PEG600, PEG1000, PEG2000 and PEG3000 solutions. The two linear lines indicate the dilute and semi-dilute regions of polymer electrolytes. d) Viscosity versus PEG M_w in a fixed concentration of 5 mg ml^{-1}. d) Adsorption layer thickness versus concentration in PEG200, PEG300 and PEG400 solutions. Inset picture, Langmuir polymer adsorption model. e) Adsorption layer thickness versus concentration in PEG600, PEG1000, PEEG2000 and PEG3000. Inset picture, multilayer polymer adsorption model. f) Adsorption layer thickness of different PEGs with a concentration of 5 mg ml^{-1} extracted from in situ QCM results.

slowing down the desorption dynamics.[8a,b,10] Simple mean-field theories,[11] as well as some experiments indicate that the number of polymer segments in the tail grows roughly as $\sqrt{M_w}$, meaning that at very high M_w, a polymer layer composed of physiosorbed molecules can be effectively considered irreversibly bonded to the substrate. Thus, either weakly adsorbed polymer layers of low M_w or weakly desorbing layers of high M_w polymers are expected to yield unstable solid-adsorbed polymer-electrolyte interphases (SPEI) at a metal anode, which is detrimental to the interfacial ion transport and metal electrodeposition morphology, etc. Taken all together, one would therefore hypothesize—on physical grounds alone, that electrodeposition at interphases formed by polymer adsorption from liquid electrolytes would exhibit optimal properties at intermediate polymer molecular weights. In other words, an optimized intermediate M_w polymer adsorption layer may be capable of creating a stable dynamic SPEI for reversible metal anodes in terms of facilitating fast interfacial ion transport, stabilizing an organic/inorganic SEI during repeated cycles of stripping and plating of the metal, suppression of parasitic reactions of electrolyte components, etc. (Figure 1a).

Results and Discussion

Interfacial adsorption of polymer chains

To evaluate this hypothesis, we first studied adsorption of polyethylene glycol (PEG) with different M_w at planar metal substrates. PEG is chosen here for at least three reasons: (1) it is soluble in most protic and aprotic electrolyte solvents used for electrochemical studies; (2) it is readily available in a range of linear chain lengths, which means that molecular weight effects can be conveniently investigated without complications from branching;[12] (3) PEG's ability to selectively adsorb on the surface of Zinc (Zn) and thereby

induce the formation of organic/inorganic SEI on the metal surface has already been reported.[7,13] To minimize transport effects caused by polymeric influences on bulk viscosity, we focus on dilute and semi-dilute polymer solutions in which the polymer has at most a small effect on ionic conductivity (see Figure S1).[14] The viscosity of neutral low M_w polymers ($M_w < 3000$ Da) in simple liquid solvents is proportional to the polymer concentration in the dilute and semi-dilute regions, respectively.[14] As illustrated in Figure 1b,c, for aqueous PEG solutions, a plot of solution viscosity, η, versus polymer concentration, c, shows that for M_w values in the range 200 Da to 3000 Da, η is a linear function of c in the dilute and semi-dilute regions, respectively. Figure 1d and Figure S2, report η as a linear function of M_w for c ranging from 3 % to 30 %.

We employed ellipsometry to measure the average adsorbate thickness formed when solutions of PEG with different concentrations and spanning a range of M_w values are exposed to a silicon wafer (Figure S3). Results reported in Figure 1e and Figure 1f show that for low M_w PEGs (PEG200, PEG300, PEG400), the average adsorbate thickness, $\bar{h}$, increases approximately linearly with c and is at most 8–10 nm for polymer concentrations considered in the study. In contrast, for higher M_w PEGs (PEG600, PEG1000, PEG2000, PEG3000), the measured $\bar{h}$ values are much larger and the relationship between $\bar{h}$ and c stronger, and nearly exponential for the highest M_w values. The different adsorption thickness trends indicate the different polymer adsorption modes.

For low M_w PEGs PEG200, PEG300, PEG400), the linear relationship between $\bar{h}$ and c can be rationalized in terms of a layer-by-layer Langmuir-type polymer adsorption model (Figure 1e inset).[15] In the Langmuir model, the different slopes apparent in Figure 1e reflect differences in adsorption/desorption frequency, in the present case indicative of a transition between the solid-like and liquid-like states of the adsorbed polymer. Consequently, the higher the frequency, the lower the slope. For higher M_w PEGs (PEG600, PEG1000, PEG2000, PEG3000), the nearly exponential increase in $\bar{h}$ with c (Figure 1f) is a reflection of collective behavior—the increasing presence of adsorbate on the substrate facilitates additional adsorption, which can be described using a multilayer polymer adsorption model (Figure 1f inset).[15a] Within this framework, the stronger exponential growth of $\bar{h}$ with c apparent in Figure 1f, can be explained straightforwardly in terms of increasing overlap of the PEG chains in solution. Based on these qualitative observations, we hypothesize that the balance of adsorption strength and interfacial impedance of SPEI produced by intermediate M_w polymers such as PEG400 would be ideal.

We used in situ Quartz Crystal Microbalance (QCM), to quantify $\bar{h}$ as a function of PEG M_w at a fixed solution concentration of 5 mg mL^{-1} polymer. The QCM experiment (Figure S4) is important because it allows polymer adsorption to be interrogated in a dynamic environment. The raw QCM data can be fitted with simple Voigt-type models for adsorbed polymers to estimate the layer thicknesses and viscosity.[7] The results summarized in Figure 1g indicate that adsorbate thickness values deduced from QCM are generally quite a bit larger than those measured using ellipsometry. The results show that PEG400 achieves the largest adsorbate thickness, compared with other polymers studied. We hypothesize that the lower adsorption thicknesses for low Mw PEGs result from high-frequency adsorption/desorption processes, which while rendering the interphases dynamic reduces their durability. In contrast, for higher Mw PEGs strong chain overlap produces cooperative (multi-chain) effects that increase the thickness and enhances the robustness of the formed interphase. At the same time, the thicker interphases would screen polymer-substrate interactions, limiting adsorbate thickness to a thermodynamics-determined value may also be altered in a dynamic flowing solution.[11a] PEG400 appears to enjoy the best of both features and was singled-out for more detailed interrogation as a spontaneous interphase former and as a convenient system for creating stable SPEI inside electrochemical cells. We first choose the aqueous Zn system as a demonstration example and then extend to a more complicated system, lithium (Li) anode, to prove the generality of the stable SPEI.

Interfacial stability of SPEI on the Zn anode

To understand the effect of SPEI composed of PEG400 on interfacial properties of metal substrates (e.g., ion transport, kinetics of side reactions, etc.), we prepared electrolytes containing low concentrations (typically 3 mg mL^{-1}) PEG. The interfacial stability of the SPEI was analyzed using a three-electrode cell that allow the metal deposition and dissolution processes to be decoupled. Figure 2a shows the structure of our three electrodes: two Zn foils are the working electrode and counter electrode, respectively, and inert silver (Ag) is the reference electrode. Figure 2b and Figure S5a report the Time-Voltage curves during cyclic stripping and plating of Zn. In this process the average voltage (vs Ag) during the deposition and strip cycle were extracted. Importantly, after each deposit or strip cycle, the apparatus allows in situ measurement of electrochemical impedance spectra (EIS) to explore the interfacial resistance change.

As shown in Figure 2c and Figure S5b, compared to the control (no PEG additive) $ZnSO_4$ (ZS) electrolytes and electrolytes containing PEG of other molecular weights, the lowest deposit and strip voltages ($\approx$0.11 V and $\approx$0.1 V, respectively) are observed for the $ZnSO_4$ + PEG400 (ZS-PEG400). Moreover, the interfacial resistance before cycling of the ZS-PEG400 electrolyte is observed to be 115±5 ohm, which is much smaller than the value for recorded using the control electrolyte (236±15 ohm) (Figure 2d), which is consistent with the lower overpotential values measured in the ZS-PEG400 electrolyte.

The in situ interfacial resistances after ten strip-plate cycles confirmed the stability of the hypothesized PEG400 SPEI formed in the ZS-PEG400 electrolyte. Figure 2d, e and Figure S6 reports the interfacial resistance during the corresponding process in the control ZS electrolyte. The varied interfacial resistances (Figure 2c, d) in different

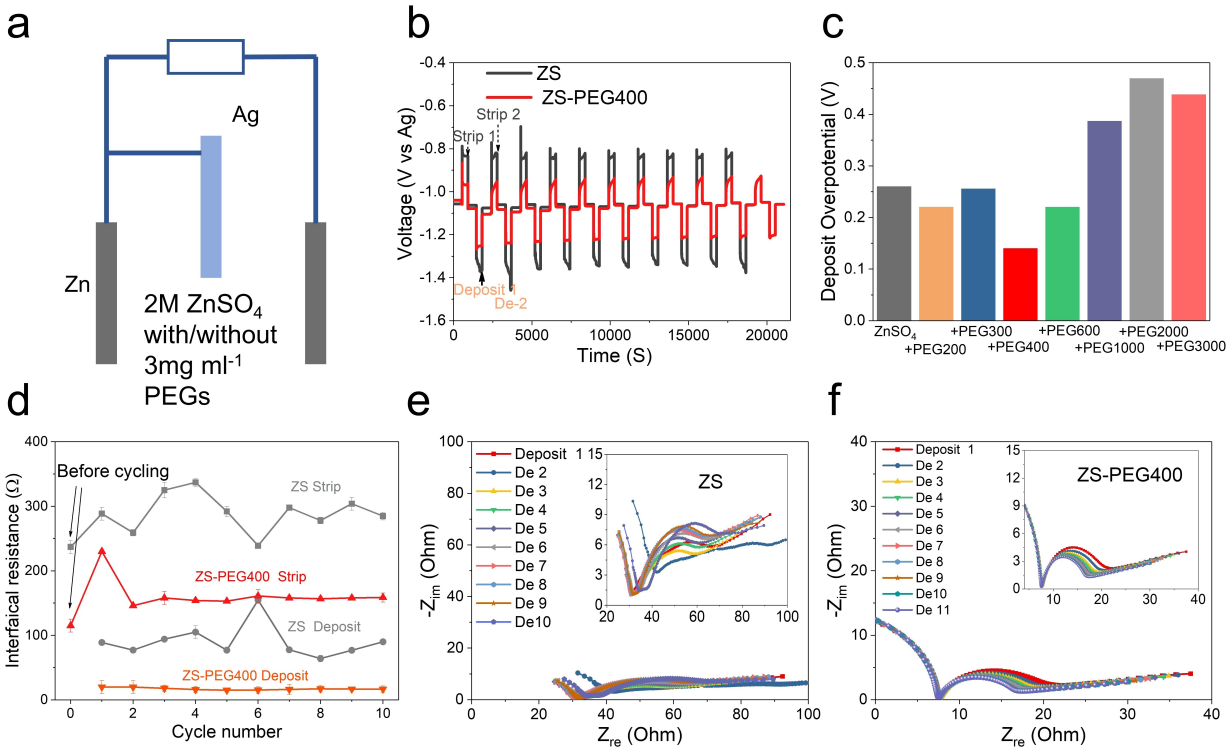

Figure 2. a) Three-electrode cell design used in the study. b) Time-voltage cycling profile for Zn in a ZS electrolyte with/without 3 mg mL^{-1} PEG400. c) Deposition voltage in ZS electrolyte as a function of PEG M_w. d) Interfacial resistance changes at different stages of ten cycles in ZS electrolytes with/without 3 mg mL^{-1} PEG400. e) In situ EIS in 2 M ZS electrolytes after each deposit step in (b). f) In situ EIS in ZS-PEG400 electrolyte after each deposit step in (b).

deposit or strip cycles are believed to result from: (1) by-product accumulation,[16] which is evidenced by the peaks of $Zn_4(OH)_6SO_4{\cdot}x\,H_2O$ in the X-ray diffraction (XRD) after cycling (Figure S7); and (2) non-uniform Zn electrodeposition morphology, as shown in Figure S8. In contrast, the interfacial resistances observed in the ZS-PEG400 system are quite stable at values of approximately 20±10 ohm at each deposit cycle and around 150±20 ohm at each strip cycle (Figure 2d, f, Figure S6). The stable interfacial impedance implies that the PEG400 SPEI is both effective in suppressing the side reactions, such as formation of $Zn_4(OH)_6SO_4{\cdot}x\,H_2O$ (Figure S7), and in regulating the Zn electrodeposition morphology (Figure S8). We note further that among the low M_w PEGs studied (PEG200, PEG300, PEG400), PEG400 exhibited the most stable interfacial resistance (Figure 2d, Figure S9). As M_w increases (PEG600, PEG1000, PEG2000, PEG3000), the interfacial resistances at each deposit and strip cycle changed markedly and unpredictably (see Figure S10 and S11), which is consistent with our previous suggestion that PEG400 forms the most stable SPEI.

Additional insights about the interfacial physical-chemistry can be obtained using a time-domain representation of the EIS data. Termed the Distribution of relaxation time (DRT) transformation of EIS results[17] (Figure S12), the method relies of a mathematical transformation to convert the frequency domain-based Nyquist plots into the time domain-based DRT spectra. This presentation is advantageous because it allows one to distinguish (at this point only qualitatively) different dynamic modes associated with physical and electrochemical processes occurring at interphases during cycling of the Zn anode in different electrolytes. As illustrated in Figure S12a and Figure S12b, dynamic processes with timescales, τ, spanning a range from hundreds of nanoseconds to tens of seconds contribute to the EIS spectra in the control ZS electrolyte. The peak τ values in the range of 10^{-7} s to 10^{-6} s are common to DRT spectra for all systems studied and are thought to reflect transport in the aqueous electrolyte component.[17b] Before the Zn anode is cycled, the peak τ values in the range of 10^{-5} s to 10s carry the richest information and are thought to reflect changes in the interfacial charge transfer process. The peak located at 1 s, for example, is apparent in the control ZS electrolyte, but is entirely absent in the ZS-PEG400 electrolyte. This change is thought to reflect fundamental differences in how electrolytes with/without PEG spontaneous corrode Zn in the ZS electrolyte. The disappearance is attributed to the retardation of chemical corrosion by the PEG400 SPEI. During Zn cycling in the control ZS electrolyte, new τ peaks emerge in the spectra, which are thought to reflect the side products formed by degradation of electrolyte components at the interface (Figure S7). A remarkable feature of the ZS-PEG400 electrolyte, is that the τ peaks found in Figure S12c and Figure S12d are coincident and stable at each deposit and

strip step, providing additional qualitative proof of the interfacial stability of the PEG400 SPEI.

Stabilizing Zn anodes using SPEIs

As shown in Figure 3a, the coulombic efficiency (CE), which is computed here from the ratio of the amount of metal that can be stripped and the amount that is plated in the previous cycle, is highly correlated to the PEG M_w. Compared to unstable SPEI of lower or higher M_w PEGs, the SPEI of the intermediate/optimum M_w PEG400 achieved the highest average CE of 98.9 % (Figure 3a, Figure S13). To further stabilize the PEG400 interphase, Br^- was introduced into the electrolyte system, as previous results[7,13,18] showed that Br^- could be specifically adsorbed to the electrode surface to form Br^- layers. Considering that PEG can bond with Br^- via Zn^{2+}-Br^- complexes,[7] we believe low concentrations of Br^- may further help stabilize the SPEI (Figure S14a). By fine-tuning the interfacial polymer adsorption through Br^-, the PEG400 SPEI was more stable, indicating by the high CE of 99.96 % in the optimized electrolyte 2 M $ZnSO_4$ + 3 mg mL^{-1} PEG400 + 0.1 M KBr (ZS-PEG400-KBr) (Figure 3a). However, a lower or higher concentration led to the decrease of the CE (Figure S14b), proving that the influence of Br^- on the SPEI is sensitive and the change of interfacial adsorption is within a small range. High CE in the optimized electrolyte enabled long cycling performance of Zn half-cells (Figure 3b, c) and symmetric cells (Figure 3d). For the Zn || carbon clothes (CC) half-cells, the cells were rapidly short circuit within a few cycles using the blank 2 M ZS electrolyte (Figure 3b). In contrast, the half-cells can run stably over 2000 cycles (Figure 3b) at high CE (≈99.96 %) using the ZS-PEG400-KBr electrolyte, which was further proved by the stable areal capacity-voltage curves in different cycles (Figure 3c). For the Zn symmetric cells, the Zn anode can stably run over 1600 hours at a high current density of 18 mA cm^{-2} and a high areal capacity of 18 mAh cm^{-2} (Figure 3d).

To further prove the application value of the optimized electrolyte system,[19] we used Zn || MnO_2 coin cells and Zn || $NaV_3O_8{\cdot}1.5H_2O$ (NVO)[20] pouch cells (Figure S15) as demonstration models. Notably, we used high loading cathode at the 3-dimensional (3D) CC for both MnO_2 cathode (≈14 mg cm^{-2}) and NVO cathode (≈16 mg cm^{-2}) to achieve high areal capacity full cells (>3 mAh cm^{-2}), which are of great importance for the practical application of Zn batteries. Furthermore, to prove the electrochemical stabil-

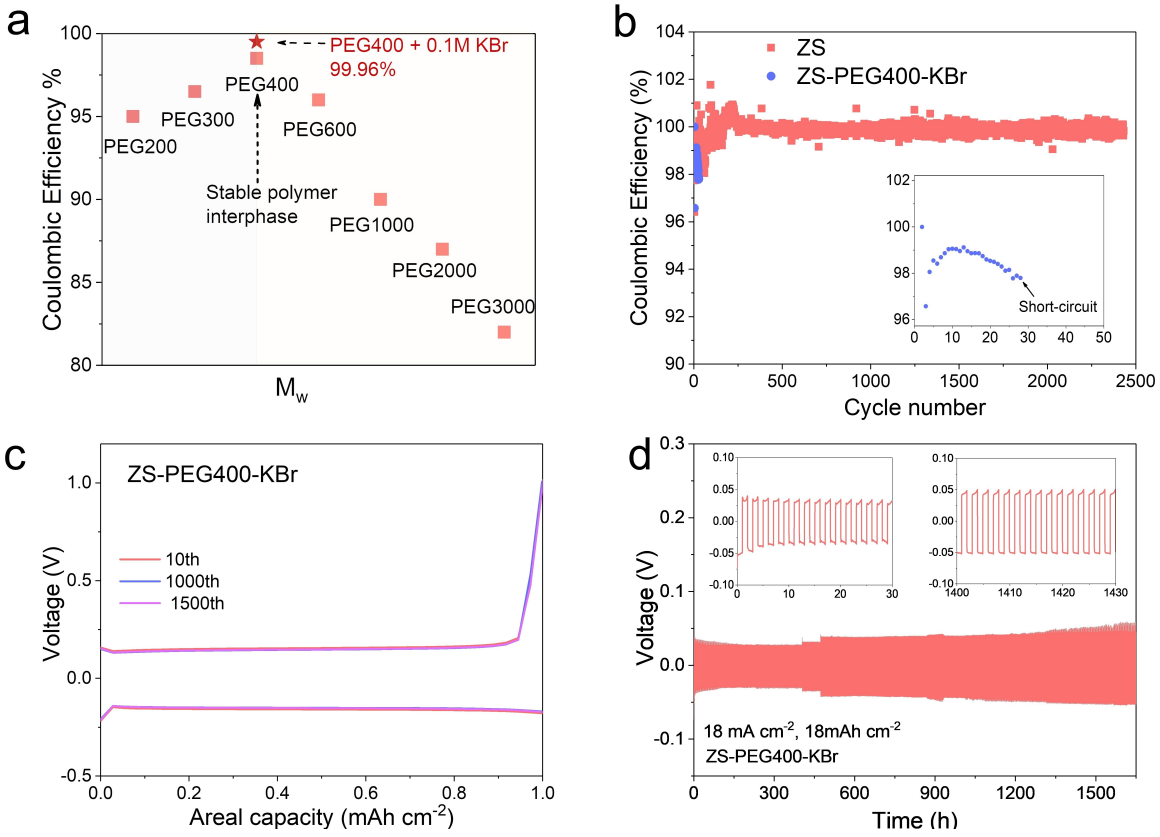

Figure 3. a) The average CE for Zn stripping/plating in electrolytes containing PEG with different Mw at a fixed concentration of 3 mg mL^{-1}. The black dashed line points out the stable polymer interphase formed by PEG400. The red star represents the CE of the optimized electrolytes 2 M $ZnSO_4$ + 3 mg mL^{-1} PEG400 + 0.1 M KBr (ZS-PEG400-KBr). b) Cycling performance of ZS-PEG400-KBr in Zn | | CC half-cells. Current density = 12 mA cm^{-2}, areal capacity = 1 mAh cm^{-2}. c) Areal capacity versus Voltage profile of Zn | | CC half-cells in (b). d) Cycling of high-capacity symmetric Zn cells in ZS-PEG400-KBr electrolytes. The insets show the voltage at different time periods. Current density = 18 mA cm^{-2}, areal capacity = 18 mAh cm^{-2}.

ity of the ZS-PEG400-KBr, a wide electrochemical window during the discharge and charge processes (0.1 V–2 V versus Zn/Zn^{2+}) was used. For Zn || MnO_2 coin cells, the battery structure was depicted in Figure 4a: the N/P ratio of 2 was achieved by depositing 9 mAh cm^{-2} Zn on CC; the E/C ratio is 5 g A^{-1} h^{-1}; the charge and discharge C rates are both 0.25 C. Moreover, 0.2 M $MnSO_4$ was added into the ZS-PEG400-KBr electrolyte to suppress the dissolution of cathode materials.[21] As Figure 4b shows, the capacity retention of Zn || MnO_2 was 20 % after 200 cycles in the blank ZS electrolyte due to the unstable SEI causing the irreversible loss of Zn deposits. However, the capacity retention was 70 % after 200 cycles in the ZS-PEG400-KBr electrolyte which should be attributed to the stable PEG400 SPEI. Moreover, the areal capacity of the full cell was still greater than 3 mAh cm^{-2} after 200 cycles in the optimized electrolyte. The areal capacity-voltage curves indicated the stability of the optimized electrolyte in different cycles (Figure 4c). For Zn || NVO pouch cells, the cell structure was depicted in Figure 4d: the N/P ratio is 3 by using thin Zn foil (20 um, 11 mAh cm^{-2}); the E/C ratio is 5 g A^{-1} h^{-1}; and the charge and discharge C rates are both 1 C. The cycling performance of the pouch cells was shown in Figure 4e: compared with the ZS electrolytes which failed within 40 cycles, the pouch cells using the ZS-PEG400-KBr electrolytes had a capacity of more than 150 mAh g^{-1} (>23 mAh) after 500 cycles, implying the good stability over the electrolyte systems. Figure 4f showed the stability of the pouch cell using ZS-PEG400-KBr electrolytes in different cycles at wide charge and discharge electrochemical windows (0.1 V–2 V versus Zn/Zn^{2+}). Taken together, the stable PEG400 SPEI shows great potential for practical applications in Zn systems due to the high areal capacity and good stability of Zn || MnO_2 coin cells and Zn || NVO pouch cells.

Adsorbed polymer induced organic/inorganic SEI formation

To in-depth understand the interphase of the interfacial polymer adsorption layer on the Zn anode, Transmission electron microscopy (TEM) and X-ray photoelectron spectroscopy (XPS) were performed to investigate the interfacial properties. As shown in Figure 5a and b, compared with the bare interphase of Zn deposits in the blank ZS electrolytes, the fresh Zn deposits are covered by a cloudy interphase layer (≈100 nm) in the ZS-PEG400 electrolytes. Moreover, with the addition of Br^-, the cloudy interphase layer changed into a dense and smooth layer, and the thickness of the interphase layer decreases from 100 nm to 50 nm (Figure 5c). The TEM results show that the fresh Zn deposits

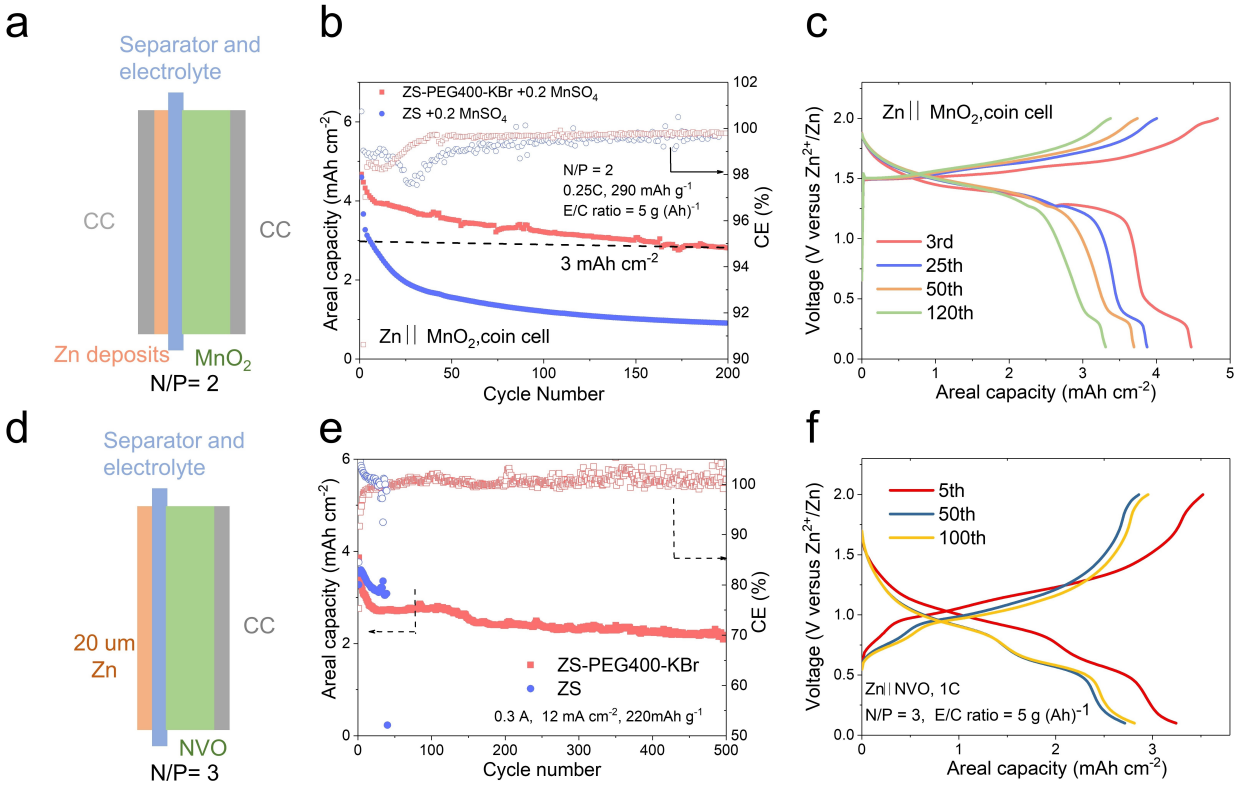

Figure 4. a) Scheme illustrating the structure of low N/P ratio Zn-MnO_2 coin cells. CC represents carbon clothes. b) Cycling performance of Zn-MnO_2 coin cells at low C rate (≈0.25 C) using the blank electrolyte and optimized electrolyte. The N/P is 2, and the E/C ratio is 5 g A^{-1} h^{-1}. The gravimetric capacity of the MnO_2 is 290 mAh g^{-1}. c) Areal Capacity-Voltage curve of the Zn-MnO_2 coin cells using ZS-PEG400-KBr electrolyte in different cycles. d) Schematic picture of the Zn-NVO pouch cells using thin Zn foil (≈20 um) and low N/P ratio. e) Cycling performance of Zn-NVO pouch cells at 1 C. The N/P is 3, and the E/C ratio is 5 g A^{-1} h^{-1}. The capacity of the Zn-NVO pouch cells is 35 mAh. f) Capacity-Voltage curve of the Zn-NVO pouch cells using ZS-PEG400-KBr electrolyte in different cycles.

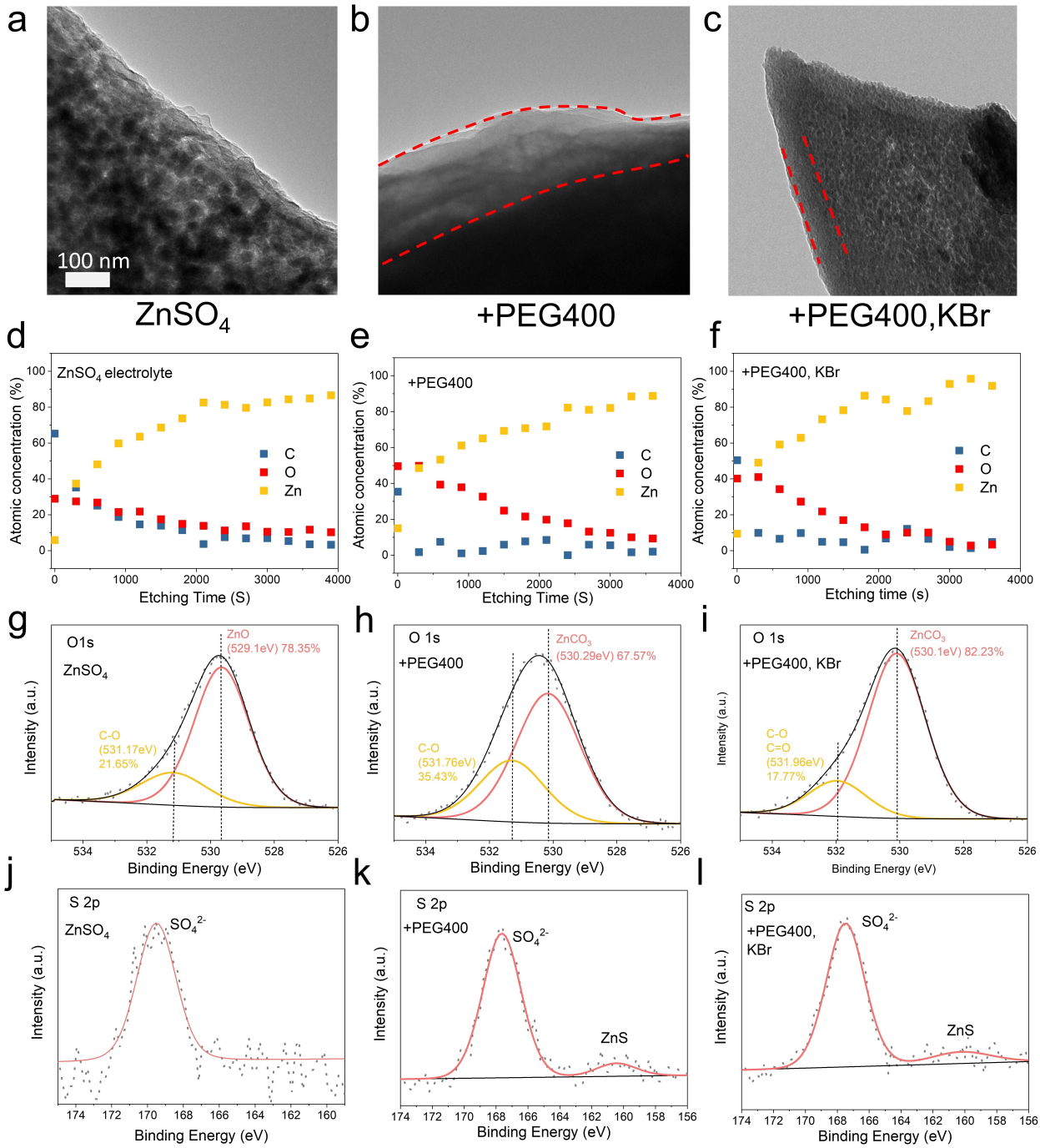

Figure 5. High-resolution TEM images of Zn deposits in a) ZS electrolytes, b) ZS-PEG400 electrolytes, c) ZS-PEG400-KBr electrolytes. Atomic concentration of C, O and Zn collected from XPS etching experiments using d) ZS electrolytes, e) ZS-PEG400 electrolytes, f) ZS-PEG400-KBr electrolytes. High-resolution XPS scan of O1s and S2p in g), j) ZS electrolytes, h), k) ZS-PEG400 electrolytes, i), l) ZS-PEG400-KBr electrolytes.

are capable of being protected by the interphase layer, which should result from the adsorption of PEG400 and is a key factor for the highly reversible and stable Zn anode.

XPS analysis was used to provide additional information about the chemical species formed on the Zn electrode surface. For the control ZS electrolytes, results from depth-resolved/sputtering XPS experiments (Figure 5d, Figure S16) show that the atomic concentration ratio between oxygen (O) and carbon (C) (O/C) is close to 1:1 at the Zn electode, which is attributed to the high ratio of the ZnO layer (78.35 %) found in the high-resolution XPS (Figure 5g). The observed high ratio ZnO layer is thought to result from the chemical and electrochemical side reactions discussed above and is considered as a source for undesirable interphase properties, such as high overpotential, dendrite growth, etc. In contrast, XPS analysis of Zn in ZS-PEG400 and ZS-PEG400-KBr electrolytes, show that the the atomic concentration of O in the PEG-induced inter-

phase increased (Figure 5e,f) is high and the atomic ratio of O/C is close to 3:1(Figure S16). This finding is revealed using the high-resolution XPS to originate from formation of a $ZnCO_3$ layer (Figure 5h, i)—the ratio of $ZnCO_3$ signals is 67.75 % and 82.23 % in the ZS-PEG400 and ZS-PEG400-KBr electrolytes, respectively (Figure 5h, i). The higher concentration of $ZnCO_3$ in the ZS-PEG400-KBr electrolytes is thought to the main source of the denser and more uniform protective SEI layer observed in complementary TEM analysis (Figure 5).

Moreover, compared with the SO_4^{2-} signal in the ZS electrolyte, ZnS peaks are observed for both the ZS-PEG400 and ZS-PEG400-KBr electrolytes studied (Figure 5k, l). On the other hand, due to the interfacial adsorption of PEG400 and Br^-, the concentration of C–O and C=O increases compared to ZS electrolytes as shown in Figure S17: the former one increases from 20.07 % (ZS electrolyte) to 25.26 % (ZS-PEG400) and 24.61 % (ZS-PEG400-KBr), and the later one increases from 10.91 % (ZS electrolyte) to 11.51 % (ZS-PEG400) and 14.36 % (ZS-PEG400-KBr), respectively. Additionally, no Br was found in the sputtering and the high sensitivity scan (Figure S18), which means that Br^- only helps and stabilizes the adsorption of PEG400 but does not participate in the formation of SEI layer. Until here, it was concluded that the bare Zn deposits in the ZS electrolytes were covered by a layer consisting of ZnO and SO_4^{2-}, which is consistent with the side products shown in the XRD. However, in the ZS-PEG400 and ZS-PEG400-KBr electrolytes, the fresh Zn deposits are capable of being protected by the organic/inorganic SEI layer consisting of $ZnCO_3$, ZnS, and PEG, etc., resulting in high reversibility and stability of Zn anode.

SPEI stability in Li anode

To evaluate the effectiveness of PEG SPEI in a very different and more complicated system, we investigated the effect of PEG additives in a 1,3-dioxolane (DOL) + 1 M LiTFSI + 0.5 M $LiNO_3$ (DOL) electrolyte. The choice of this DOL electrolytes is admittedly a compromise made to preemptively address the known, limited electrochemical stability (<4 V vs Li/Li^+) of low-molecular-weight PEG molecules of interest in this study at a Li anode. Figure 6a reports the effect of different PEG M_w on the CE for Li deposit/strip process in the DOL electrolyte at a fixed (2 mg mL^{-1}) PEG concentration. The effect of PEG MW on CE is—surprisingly—consistent with our earlier observations of Zn in aqueous electrolytes; again, the PEG400 additive is found to yield the highest CE value of approximately 99 %. The higher CE produced by the PEG400 additive is also seen to extend cycling lifetime for Li||Cu half-cells (Figure 6b). The benefits of the PEG400 SPEI are

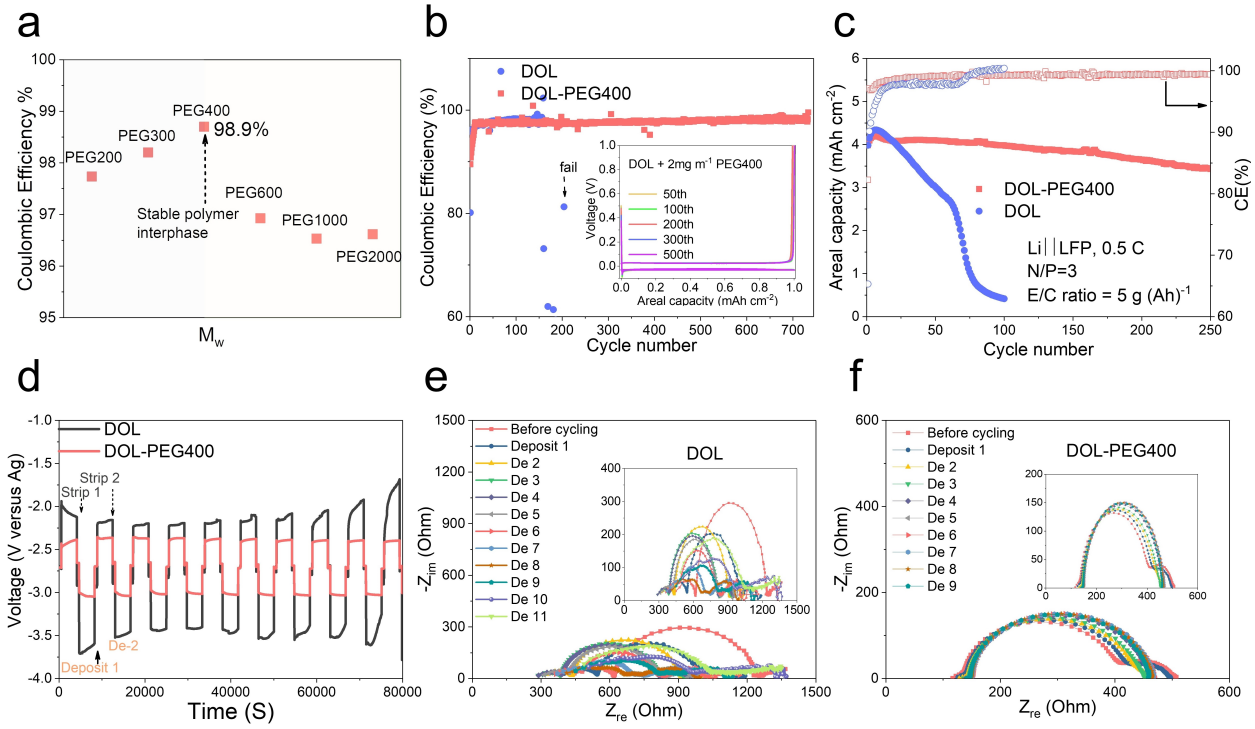

Figure 6. a) The average CE in DOL + 2 mg mL^{-1} PEG electrolytes. b) Cycling performance of optimized electrolytes DOL + 1 M LiTFSI + 0.5 M $LiNO_3$ + 2 mg mL^{-1} PEG400 (DOL-PEG400) in Li||Cu half-cells. 1 mA cm^{-2}, 1 mAh cm^{-2}. Inset picture, Areal Capacity-Voltage curves in different cycles. c) Cycling performance of high areal capacity Li||LFP full cells in DOL electrolytes with/without 2 mg mL^{-1} PEG400. The N/P ratio is 3, and the E/C ratio is 5 g A^{-1} h^{-1}. d) Time-Voltage cycling profile in three-electrode cells using DOL electrolyte with/without 2 mg mL^{-1} PEG400. 1 mA cm^{-2}, 1 mAh cm^{-2}. e) In situ EIS in DOL electrolyte after each deposit step in (d). f) In situ EIS in DOL-PEG400 electrolyte after each deposit step in (d).

also apparent in the capacity-voltage curve measured at different cycles provided as an inset to Figure 6b.

As a final evaluation, we created Li || LFP full cells using the DOL-based electrolyte containing PEG400 additive. The results reported in Figure 6c show that PEG400 produce quite large improvements in performance at reasonable capacities of 4 $mAh\,cm^{-2}$. As an even more aggressive test of the PEG400 additive, we created Li || LFP full cells with the N/P ratio of 3 and E/C ratio is 5 $g\,A^{-1}\,h^{-1}$ by depositing 12 $mAh\,cm^{-2}$ Li on Cu. The cells were evaluated at a fixed charge and discharge rate of 0.5 C. For the control DOL electrolyte, the capacity retention is about 12 % after 100 cycles. As shown in the capacity-voltage curves (Figure S19), voltage polarization during the cell cycling increased greatly, which is thought to result from the unstable SEI formed at the anode side.[1d] Nevertheless, the DOL + 2 $mg\,mL^{-1}$ PEG400 (DOL-PEG400) electrolyte shows a good stability over 250 cycles, in which capacity retention was 87.5 %. The charge and discharge voltages were also stable in different cycles (Figure S19) due to the stable PEG400 SPEI. To prove the stability of PEG400 SPEI, interfacial properties of the Li anode were analyzed using three-electrode experiments. As Figure 6d shows, the deposit/strip overpotential extracted from the three-electrode experiments decreased from 0.75 V of blank DOL electrolytes to 0.25 V of DOL-PEG400 electrolytes. On the other hand, compared to unpredictable interfacial resistance changes in blank DOL electrolyte, with the stable PEG400 SPEI (Figure 6e, f, Figure S20 and S21), the interfacial resistances after each strip and deposit cycle were constant and stable (321±10 ohm, 320±13 ohm, respectively), implying that the PEG400 was capable of stabilizing the interfacial properties by constructing a stable SPEI as what we found in the Zn systems. DRT transformation of EIS data provide even more dramatic evidence (see Figure S22) than for the Zn case and in support of the effectiveness of a PEG 400 SPEI in stabilizing a Li anode. Specifically, compared with multiple τ peaks in the control DOL electrolytes—attributed to different electrochemical side reactions after depositing and stripping Li, only one dominant τ peak at around 5 μs was found in the DOL-PEG400 electrolytes, which we attribute to ion transport in the PEG400 SPEI. While much more work is needed to make this assignment concrete, the "quietness" of the DRT spectrum produced by the PEG400 SPEI is an important discovery deserving of more in-depth studies.

Conclusion

In summary, we report that spontaneous adsorption of low-molecular weight PEG molecules on Li and Zn metal anodes provides a facile route towards creating robust interphases that enhance electrode reversibility. We studied the adsorption states of PEGs with different M_w via thickness adsorption measurements, which enables us to deduct the most stable polymer adsorption interphase—PEG400. Additionally, through in situ EIS, and other electrochemical experiments, we demonstrated that the PEG400 SPEI can stabilize the interfacial properties (e.g. interfacial ion transport, suppression of side reactions, etc.) by forming an organic/inorganic SEI layers, which further leads to highly reversible Zn and Li anodes. Finally, we evaluate the interphases in high-performance full cells with low N/P and E/C ratios, and high areal capacity. Studies performed both in aqueous Zn systems and non-aqueous Li systems reveal that the in situ formed polymeric SPEI are beneficial for extending cycle life.

Data Availability

All datasets generated and analyzed during the current study are available from the corresponding author (LAA) upon reasonable request.

Acknowledgements

This work was supported by DOE BES under award # DE-SC0016082 and as part of the Center for Mesoscale Transport Properties, an Energy Frontier Research Center supported by the U.S. Department of Energy, Office of Science, Basic Energy Sciences, under award #DE-SC0012673. The work made use of the Cornell Center for Materials Research Shared Facilities which are supported through the NSF MRSEC program (DMR-1719875).

Conflict of Interest

The authors declare no competing interests.

Data Availability Statement

The data that support the findings of this study are available from the corresponding author upon reasonable request.

Keywords: Adsorbed Polymer Interphases · Aqueous Zn Battery · Li Metal Battery · Polymer-Induced Organic/Inorganic SEI

[1] a) M. D. Tikekar, S. Choudhury, Z. Tu, L. A. Archer, *Nat. Energy* **2016**, *1*, 1–7; b) M. J. Zachman, Z. Tu, S. Choudhury, L. A. Archer, L. F. Kourkoutis, *Nature* **2018**, *560*, 345–349; c) L. Cao, D. Li, T. Pollard, T. Deng, B. Zhang, C. Yang, L. Chen, J. Vatamanu, E. Hu, M. J. Hourwitz, L. Ma, M. Ding, Q. Li, S. Hou, K. Gaskell, J. T. Fourkas, X. Q. Yang, K. Xu, O. Borodin, C. Wang, *Nat. Nanotechnol.* **2021**, *16*, 902–910; d) Z. Zhang, Y. Li, R. Xu, W. Zhou, Y. Li, S. T. Oyakhire, Y. Wu, J. Xu, H. Wang, Z. Yu, D. T. Boyle, W. Huang, Y. Ye, H. Chen, J. Wan, Z. Bao, W. Chiu, Y. Cui, *Science* **2022**, *375*, 66–70; e) C. Li, A. Shyamsunder, A. G. Hoane, D. M. Long, C. Y. Kwok, P. G. Kotula, K. R. Zavadil, A. A. Gewirth, L. F. Nazar, *Joule* **2022**, *6*, 1103–1120; f) Y. Liu, X. Tao, Y. Wang, C. Jiang, C. Ma, O. Sheng, G. Lu, X. W. D. Lou, *Science* **2022**, *375*, 739–745; g) Y. Li, Y. Li, A. Pei, K. Yan, Y. Sun, C.-L. Wu, L.-M.

Joubert, R. Chin, A. L. Koh, Y. Yu, J. Perrino, B. Butz, S. Chu, Y. Cui, *Science* **2017**, *358*, 506–510.
[2] a) Q. Zhao, S. Stalin, L. A. Archer, *Joule* **2021**, *5*, 1119–1142; b) X. Shen, R. Zhang, X. Chen, X. B. Cheng, X. Li, Q. Zhang, *Adv. Energy Mater.* **2020**, *10*, 1903645; c) B. Han, Y. Zou, G. Xu, S. Hu, Y. Kang, Y. Qian, J. Wu, X. Ma, J. Yao, T. Li, *Energy Environ. Sci.* **2021**, *14*, 4882–4889; d) S. Jurng, Z. L. Brown, J. Kim, B. L. Lucht, *Energy Environ. Sci.* **2018**, *11*, 2600–2608.
[3] M. S. Kim, J.-H. Ryu, Deepika, Y. R. Lim, I. W. Nah, K.-R. Lee, L. A. Archer, W. I. Cho, *Nat. Energy* **2018**, *3*, 889–898.
[4] a) E. Cha, M. D. Patel, J. Park, J. Hwang, V. Prasad, K. Cho, W. Choi, *Nat. Nanotechnol.* **2018**, *13*, 337–344; b) M. S. Kim, Deepika, S. H. Lee, M.-S. Kim, J.-H. Ryu, K.-R. Lee, L. A. Archer, W. I. Cho, *Sci. Adv.* **2019**, *5*, eaax5587.
[5] a) K. Liu, A. Pei, H. R. Lee, B. Kong, N. Liu, D. Lin, Y. Liu, C. Liu, P. C. Hsu, Z. Bao, Y. Cui, *J. Am. Chem. Soc.* **2017**, *139*, 4815–4820; b) J. Lopez, A. Pei, J. Y. Oh, G. N. Wang, Y. Cui, Z. Bao, *J. Am. Chem. Soc.* **2018**, *140*, 11735–11744; c) W. Zhang, H. L. Zhuang, L. Fan, L. Gao, Y. Lu, *Sci. Adv.* **2018**, *4*, eaar4410; d) S. Stalin, P. Chen, G. Li, Y. Deng, Z. Rouse, Y. Cheng, Z. Zhang, P. Biswal, S. Jin, S. P. Baker, R. Yang, L. A. Archer, *Matter* **2021**, *4*, 3753–3773; e) W. Zhang, Q. Zhao, Y. Hou, Z. Shen, L. Fan, S. Zhou, Y. Lu, L. A. Archer, *Sci. Adv.* **2021**, *7*, eabl3752; f) A.-L. Chen, N. Shang, Y. Ouyang, L. Mo, C. Zhou, W. W. Tjiu, F. Lai, Y.-E. Miao, T. Liu, *eScience* **2022**, *2*, 192–200; g) Y. Lv, M. Zhao, Y. Du, Y. Kang, Y. Xiao, S. Chen, *Energy Environ. Sci.* **2022**, *15*, 4748–4760.
[6] X. Wei, M. Nyce, G. G. Yadav, A. Couzis, S. Banerjee, U.S. Patent 674, **2021**.
[7] S. Jin, J. Yin, X. Gao, A. Sharma, P. Chen, S. Hong, Q. Zhao, J. Zheng, Y. Deng, Y. L. Joo, L. A. Archer, *Nat. Commun.* **2022**, *13*, 2283.
[8] a) V. S. Minnikanti, Z. Qian, L. A. Archer, *J. Chem. Phys.* **2007**, *126*, 144905; b) V. S. Minnikanti, L. A. Archer, *Macromolecules* **2006**, *39*, 7718–7728; c) J. Han, S. W. Turner, H. G. Craighead, *Phys. Rev. Lett.* **1999**, *83*, 1688.
[9] M. A. Cohen Stuart, T. Cosgrove, B. Vincent, *Adv. Colloid Interface Sci.* **1985**, *24*, 143–239.
[10] a) Z. Qian, V. S. Minnikanti, L. A. Archer, *J. Polym. Sci. Part B* **2008**, *46*, 1788–1801; b) Z. Qian, V. S. Minnikanti, B. B. Sauer, G. T. Dee, L. A. Archer, *Macromolecules* **2008**, *41*, 5007–5013.
[11] a) E. Bouchaud, M. Daoud, *J. Phys.* **1987**, *48*, 1991–2000; b) P. G. de Gennes, P. Pincus, *J. Phys. Lett.* **1983**, *44*, 241–246.
[12] a) S. J. Banik, R. Akolkar, *J. Electrochem. Soc.* **2013**, *160*, D519; b) A. Mitha, A. Z. Yazdi, M. Ahmed, P. Chen, *ChemElectroChem* **2018**, *5*, 2409–2418.
[13] S. Jin, D. Zhang, A. Sharma, Q. Zhao, Y. Shao, P. Chen, J. Zheng, J. Yin, Y. Deng, P. Biswal, L. A. Archer, *Small* **2021**, *17*, 2101798.
[14] R. Lambourne, T. A. Strivens, *Paint and Surface Coatings*, Elsevier, Amsterdam, **1999**.
[15] a) Y. Liu, X. Fan, X. Jia, B. Zhang, H. Zhang, A. Zhang, Q. Zhang, *J. Mater. Sci.* **2016**, *51*, 8579–8592; b) W. Huang, S. Pan, Q. Yu, X. Liu, Y. Liu, R. Liu, *J. Inorg. Organomet. Polym. Mater.* **2019**, *29*, 1755–1766.
[16] a) H. Yu, Y. Zeng, N. W. Li, D. Luan, L. Yu, X. W. D. Lou, *Sci. Adv.* **2022**, *8*, eabm5766; b) Y. Zeng, P. X. Sun, Z. Pei, Q. Jin, X. Zhang, L. Yu, X. W. D. Lou, *Adv. Mater.* **2022**, *34*, 2200342; c) L. Ma, Q. Li, Y. Ying, F. Ma, S. Chen, Y. Li, H. Huang, C. Zhi, *Adv. Mater.* **2021**, *33*, 2007406.
[17] a) F. Dion, A. Lasia, *J. Electroanal. Chem.* **1999**, *475*, 28–37; b) Y. Lu, C.-Z. Zhao, R. Zhang, H. Yuan, L.-P. Hou, Z.-H. Fu, X. Chen, J.-Q. Huang, Q. Zhang, *Sci. Adv.* **2021**, *7*, eabi5520; c) Y. Lu, C.-Z. Zhao, J.-Q. Huang, Q. Zhang, *Joule* **2022**, *6*, 1172–1198.
[18] W. Zhang, Y. Lu, L. Wan, P. Zhou, Y. Xia, S. Yan, X. Chen, H. Zhou, H. Dong, K. Liu, *Nat. Commun.* **2022**, *13*, 2029.
[19] a) G. Zampardi, F. La Mantia, *Nat. Commun.* **2022**, *13*, 687; b) C. Li, S. Jin, L. A. Archer, L. F. Nazar, *Joule* **2022**, *6*, 1733–1738.
[20] F. Wan, L. Zhang, X. Dai, X. Wang, Z. Niu, J. Chen, *Nat. Commun.* **2018**, *9*, 1656.
[21] H. Pan, Y. Shao, P. Yan, Y. Cheng, K. S. Han, Z. Nie, C. Wang, J. Yang, X. Li, P. Bhattacharya, K. T. Mueller, J. Liu, *Nat. Energy* **2016**, *1*, 16039.

Manuscript received: January 16, 2023
Accepted manuscript online: March 2, 2023
Version of record online: March 22, 2023